AIAA-92-0190

Multigrid Navier-Stokes Calculations For Three-dimensional Cascades

F. Liu and A. Jameson
Princeton University
Princeton, NJ

30th Aerospace Sciences Meeting & Exhibit

January 6-9, 1992 / Reno, NV

Multigrid Navier-Stokes Calculations for Three Dimensional Cascades

Feng Liu* and Antony Jameson†
Department of Mechanical and Aerospace Engineering
Princeton University, Princeton, NJ

Abstract

A vertex-based finite volume method for solving the three-dimensional compressible Reynolds-averaged Navier-Stokes equations is presented for calculating turbomachinery cascade flows. A discretization scheme for the viscous terms is proposed. This discretization scheme avoids a potential problem on kinked meshes. The Baldwin-Lomax algebraic turbulence model is used. The scheme is verified against laminar and turbulent flows over a flat plate. Perfect agreement is obtained with the Blasius solution for the laminar flow. Agreement with empirical solutions is also obtained for turbulent flows. Both two- and three-dimensional computations were carried out for a low pressure turbine cascade. Results are compared with inviscid solutions and experimental data. Predicted pressure distributions agree with experiments at both design and off-design conditions. Surface skin-friction distribution and velocity vectors in the flow field are also presented.

1 Introduction

With the advent of computer technology and numerical methods, flow field computations of turbomachinery cascades become feasible as a routine design procedure. In many cases a good prediction of blade pressure distributions can be achieved by using an inviscid method, eg. Denton[1], Smith and Caughey[2], Holmes and Tong[3], and Liu and Jameson[4, 5]. However, since such a method ignores viscous effects it may fail badly in predicting off-design conditions. Under such conditions, viscous effects such as boundary layer separation may have drastic effects on the pressure distribution on the cascade blades.

In an earlier paper[5] the authors presented results of cascade flow calculations with a three-dimensional Euler method. It was found that the pressure distribution on the cascade blade surface agreed well with the experimental data obtained by Hodson and Dominy[11, 12, 13] for a low pressure turbine cascade at its design condition. When proper inlet boundary conditions were given the Euler equations were also found to be capable of capturing the major features of secondary flow vortices caused by the convection of the inlet endwall boundary layers. However, small discrepancies existed where small separation bubbles were found in experiment at the design condition. At an off-design condition there were large differences between the predicted pressure distributions and the experimental data due to the existence of large separation in the flow field. For such flows it is essential to include viscous effects in the simulation. Solution of the Navier-Stokes equations is particularly needed for flows with strong blade and endwall interactions. Hah developed an implicit relaxation method for the Navier-Stokes equations[6]. Chima used an explicit multigrid algorithm for quasi-three-dimensional flows[7]. Some other contributions include Davis, Ni and Carter[8], Choi and Knight[9], and Dawes[10].

In this paper a finite volume scheme for solving the Reynolds-averaged Navier-Stokes equations in three dimensions is presented. A vertex scheme is used in this work instead of the cell-centered scheme used in [5] for the Euler equations. It is believed that a cell-vertex scheme may have better accuracy than a cell-centered scheme on irregular meshes. In this paper an alternative discretization is used for the viscous terms as modified from one of the schemes used by Martinelli[16] in his two-dimensional Navier-Stokes code. This new discretization avoids a potential difficulty in calculating the viscous terms when the computational mesh has kinks. A multigrid method is used to accelerate convergence. The numerical method with the Baldwin-Lomax algebraic turbulence model is used to calculate the flow in the same low pressure turbine cascade[11, 12, 13] for which solutions of the Euler equations were obtained by the authors in [5]. The usefulness and limitations of the Navier-Stokes calculations will be demonstrated through comparison of the results with those of the Euler calculations and the experiment.

---

*Research Assistant, Member AIAA, Current address: Department of Mechanical and Aerospace Engineering, University of California, Irvine, CA 92717

†Professor, Member AIAA.

2 Numerical Method

2.1 The Reynolds-averaged Navier-Stokes equations

After proper non-dimensionalization, the Reynolds-averaged Navier-Stokes equations can be written in an integral form as

$$\frac{d}{dt}\int_{\Omega}\mathbf{W}dt+\oint_{S}\vec{\mathbf{f}}\cdot\vec{n}dS=\frac{1}{Re}\oint_{S}\vec{\mathbf{F}}\cdot\vec{n}dS \qquad (1)$$

for a fixed region Ω, where

$$\mathbf{W}=\{W_l\}=\begin{bmatrix}\rho\\ \rho u\\ \rho v\\ \rho w\\ \rho E\end{bmatrix} \qquad (2)$$

$$\vec{\mathbf{f}}=\{\vec{f_l}\}=\{f_{l,j}\}=\begin{bmatrix}\rho u_j\\ \rho u_i u_j+p\delta_{ij}\\ (i=1,2,3)\\ (\rho E+p)u_j\end{bmatrix} \qquad (3)$$

$$\vec{\mathbf{F}}=\{\vec{F_l}\}=\{F_{l,j}\}=\begin{bmatrix}0\\ \sigma_{ij}\\ (i=1,2,3)\\ u_i\sigma_{ij}-q_j\end{bmatrix} \qquad (4)$$

and $\vec{V}=\{u_1,u_2,u_3\}=\{u,v,w\}$ is the velocity vector.

$\mathbf{W}$ is a formal vector of 5 scalar components: w_l, where $l=1,2,\ldots,5$ indicates the equation number in the Navier-Stokes system of equations; $\vec{\mathbf{f}}$ and $\vec{\mathbf{F}}$ are formal vectors of 5 cartesian vector components: $\vec{f_l}$ and $\vec{F_l}$; The bold face here is used to denote that $\mathbf{W}$, $\vec{\mathbf{f}}$, and $\vec{\mathbf{F}}$ are pseudo vectors in l. The arrowed overscores, however, indicate that $\vec{\mathbf{f}}$ and $\vec{\mathbf{F}}$ are *genuine cartesian vectors in space*. Re is the Reynolds number based on the reference values in the non-dimensionalization.

$$Re=\frac{\rho_{ref}V_{ref}l_{ref}}{\mu_{ref}}=\frac{1}{\sqrt{\gamma}M_{\infty}}Re_{\infty} \qquad (5)$$

where

$$Re_{\infty}=\frac{\rho_{\infty}V_{\infty}l_{\infty}}{\mu_{\infty}} \qquad (6)$$

The eddy viscosity concept due to Boussinesq is used for turbulent flow. The total stress is related to the the mean shear stress by a total viscosity coefficient: $\mu+\mu_t$

$$\sigma_{ij}=2(\mu+\mu_t)S_{ij}-\frac{2}{3}(\mu+\mu_t)\frac{\partial u_k}{\partial x_k}\delta_{ij} \qquad (7)$$

where S_{ij} is the rate of strain tensor, μ is the molecular viscosity, and μ_t is the turbulent eddy viscosity.

Similarly, the total heat flux is related to the temperature gradient as in the Fourier law by a total heat conductivity: $k+k_t$

$$q_j=-(k+k_t)\nabla T \qquad (8)$$

where k is the molecular heat conductivity and k_t is the turbulent heat conductivity.

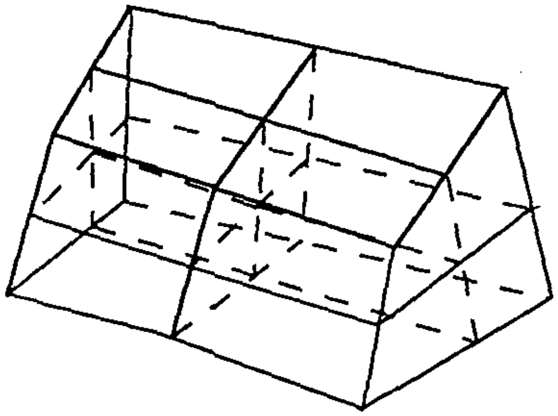

Figure 1: A Three-dimensional Super-cell for the Vertex Scheme

2.2 Finite Volume Scheme and Time Stepping

The basic numerical method is described in more detail in [15]. The computational domain is divided into hexahedral cells. In a vertex scheme the flow variables are defined at the cell-vertices of hexahedral cells. A system of ordinary differential equations can be obtained by applying equation (1) to a super-cell formed by the union of 8 cells surrounding a vertex point as shown in Fig. 1.

$$\frac{d}{dt}(\Omega_{ijk}\mathbf{W}_{ijk})+\mathbf{Q}_{c,ijk}-\mathbf{Q}_{\nu,ijk}=0 \qquad (9)$$

where Ω_{ijk} is the volume of the super-cell, $\mathbf{Q}_{c,ijk}$, $\mathbf{Q}_{\nu,ijk}$ are the net convective and diffusive fluxes out of the super-cell, respectively. The convective flux balance over the m-th elementary cell around the vertex (i,j,k) can be approximated by

$$(\mathbf{Q}_{c,ijk})_m=\sum_{k=1}^{6}\vec{\mathbf{f}}_k\cdot d\vec{S}_k \quad \text{for } m=1,2,\cdots,8 \qquad (10)$$

where the summation is over the six faces of the hexahedral cell. $d\vec{S}_k=\vec{n}\cdot dS_k$ is the face area vector, which has the face area as its magnitude and the outer normal $\vec{n}$ for its direction. $\vec{\mathbf{f}}_k$ are the average flux vectors on each face. The convective flux balance over one super-cell can be obtained by summing the flux balances over the 8 constituent cells.

$$\mathbf{Q}_{c,ijk}=\sum_{m=1}^{8}(\mathbf{Q}_{c,ijk})_m \qquad (11)$$

Since flow variables are defined at cell-vertices, the velocity and temperature derivatives at each cell

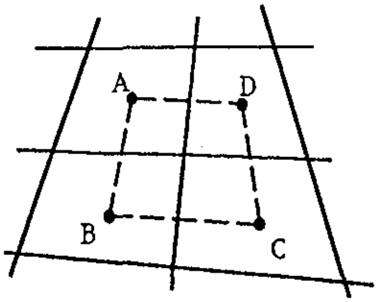

Figure 2: Martinelli's Auxiliary Cell to Calculate Derivatives for the Cell-centered Scheme

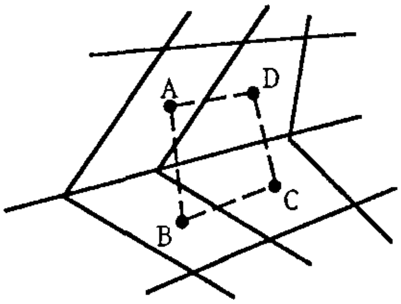

Figure 3: Problem with a Kinked Mesh

center can be found by applying Gauss's formula to each individual cell. Suppose $\frac{\partial u}{\partial x}$ is to be found at the center of a cell. By Gauss's formula,

$$\int_{\Omega} \frac{\partial u}{\partial x} = \int_{\partial\Omega} u dS_x$$

thus,

$$\Omega \frac{\partial u}{\partial x} \approx \int_{\partial\Omega} u dS_x$$

where dS_x is the x component of $d\vec{S}$.

To calculate the viscous fluxes $\mathbf{Q}_{\nu,ijk}$ an auxiliary control volume around the vertex point (i,j,k) is formed. For simplicity, consider in Fig. 2 a vertex point in a two-dimensional mesh. Martinelli[16] in one of his two-dimensional schemes formed the auxiliary control volume by directly connecting the cell-centers A, B, C, and D(Fig. 2). Since the derivatives of velocity and temperature are found at all cell centers, $\vec{\mathbf{F}}_k$ on each face of the above formed control volume can be evaluated as the average of $\vec{\mathbf{F}}$ at the end points. $\mathbf{Q}_{\nu,ijk}$ can then be obtained by

$$\mathbf{Q}_{\nu,ijk} = \sum_{k=1}^{6} \vec{\mathbf{F}}_k \cdot d\vec{S}_k \qquad (12)$$

A difficulty may arise, however, in the above method when the mesh exhibits a kink as shown in Fig. 3. In that case, the vertex point where the diffusive flux balance is to be found falls outside the auxiliary cell and the local accuracy may drop. To rectify this, an alternative scheme is proposed. An auxiliary cell connecting A, B, C, D, and the mid-points(mid-lines in three-dimensions) a, b, c, and d of the cell faces is formed as shown in Fig. 4.

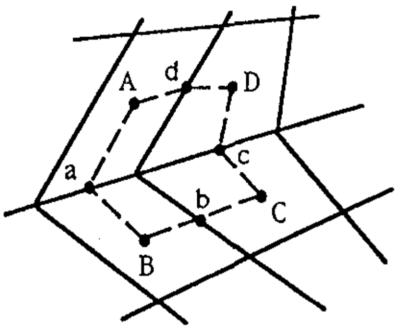

Figure 4: Auxiliary Cell used in This Work to Calculate the Diffusive Balance for the Cell-vertex Scheme

The surface integral on face Aa can be evaluated as $\vec{\mathbf{F}}_A$ times $(d\vec{S})_{Aa}$, where $\vec{\mathbf{F}}_A$ is $\vec{\mathbf{F}}$ at A and $(d\vec{S})_{Aa}$ is surface area vector for Aa. The surface integrals over other face segments of the control volume in Fig. 4 can be formed in the same manner. Although the surface integral on each face segment is one-sided, the above scheme is equivalent to Martinelli's scheme for regular meshes but is expected to give better local accuracy on grids with sharp kinks.

With the above formulation, we have associated with each vertex, on which flow variables are defined, a control volume(the super-cell) to which the integral equation (1) is applied, thus producing equal numbers of equations and unknowns. It appears, however, that two different control volumes have been used for the convective and diffusive terms in the above approach. This can be reconciled by scaling the magnitude of $\mathbf{Q}_{c,ijk}$ so that it corresponds to that for the control volume used to calculate $\mathbf{Q}_{\nu,ijk}$ or vice versa. The schemes thus constructed for the convective and diffusive terms are both separately globally conservative, with the consequence that global conservation of mass, momentum and energy is assured.

The above scheme reduces to a central difference scheme on Cartesian meshes, and is second order accurate if the mesh is sufficiently smooth. However a central difference scheme will permit modes with odd and even decoupling. To prevent this and to capture shocks without pre-shock oscillations, an additional dissipation term is added to the semi-discrete equation (9) so that we solve

$$\frac{d}{dt}(\Omega_{ijk}\mathbf{W}_{ijk}) + \mathbf{Q}_{ijk} - \mathbf{D}_{ijk} = 0 \qquad (13)$$

where

$$\mathbf{Q}_{ijk} = \mathbf{Q}_{c,ijk} + \mathbf{Q}_{\nu,ijk}$$

$$\mathbf{D}_{ijk} = (D_\xi + D_\eta + D_\zeta)\mathbf{W}_{ijk}$$

and

$$D_\xi \mathbf{W}_{ijk} = \mathbf{d}_{i+\frac{1}{2},j,k} - \mathbf{d}_{i-\frac{1}{2},j,k} \quad .$$

The *dissipation* fluxes $\mathbf{d}_{i+\frac{1}{2},j,k}$ are defined as a blending of first and third differences

$$\begin{aligned} \mathbf{d}_{i+\frac{1}{2},j,k} &= \epsilon^{(2)}_{i+\frac{1}{2},j,k}(R_\xi)_{i+\frac{1}{2},j,k}\Delta_\xi \mathbf{W}_{i,j,k} \\ &+ \epsilon^{(4)}_{i-\frac{1}{2},j,k}(R_\xi)_{i+\frac{1}{2},j,k}\Delta^3_\xi \mathbf{W}_{i-1,j,k} \end{aligned}$$

where Δ_ξ is the forward difference operator defined by

$$\Delta_\xi \mathbf{W}_{ijk} = \mathbf{W}_{i+1,j,k} - \mathbf{W}_{ijk} \quad .$$

In the current method for the Reynolds-averaged equations, redistributed directionally variable dissipation scales are used following Martinelli's work in two-dimensions. In this approach

$$(R_\xi)_{i+\frac{1}{2},j,k} = \lambda_\xi \Phi$$

where

$$\Phi = 1 + \max\left\{\left(\frac{\lambda_\eta}{\lambda_\xi}\right)^\omega, \left(\frac{\lambda_\zeta}{\lambda_\xi}\right)^\omega\right\}$$

ω is a parameter usually chosen to be 0.66. λ_ξ, λ_η and λ_ζ are the spectral radii of the Jacobian matrices of $\vec{\mathbf{f}} \cdot \vec{S}_\xi$, $\vec{\mathbf{f}} \cdot \vec{S}_\eta$ and $\vec{\mathbf{f}} \cdot \vec{S}_\zeta$, respectively, where $\vec{S}_\xi$, $\vec{S}_\eta$ and $\vec{S}_\zeta$ are the cell surface area vectors along each grid line direction. Exactly similar terms can be constructed for $D_\eta \mathbf{W}_{ijk}$ and $D_\zeta \mathbf{W}_{ijk}$.

Equation (13) can then be written as

$$\frac{d\mathbf{W}_{ijk}}{dt} + \mathbf{R}_{ijk}(\mathbf{W}) = 0 \quad , \tag{14}$$

where $\mathbf{R}_{ijk}$ is the residual

$$\mathbf{R}_{ijk}(\mathbf{W}) = \frac{1}{\Omega_{ijk}}(\mathbf{Q}_{ijk} - \mathbf{D}_{ijk}) \quad .$$

Eqn. (14) can be integrated in time by an explicit multistage scheme. Let $\mathbf{W}^n$ be the value of $\mathbf{W}_{ijk}$ after n time steps. Dropping the subscripts i, j, k a general m stage hybrid scheme to advance a time step Δt can be written as

$$\begin{array}{lclcrl} \mathbf{W}^{(0)} & = & \mathbf{W}^n & & & \\ \mathbf{W}^{(1)} & = & \mathbf{W}^{(0)} & - & \alpha_1 & \Delta t \mathbf{R}^{(0)} \\ & \cdots & & & & \\ \mathbf{W}^{(m-1)} & = & \mathbf{W}^{(0)} & - & \alpha_{m-1} & \Delta t \mathbf{R}^{(m-2)} \\ \mathbf{W}^{(m)} & = & \mathbf{W}^{(0)} & - & & \Delta t \mathbf{R}^{(m-1)} \\ \mathbf{W}^{n+1} & = & \mathbf{W}^{(m)} & & & \end{array}$$

In this implementation a 5 stage scheme is used with evaluations of the dissipation and the viscous terms only at the first, third and fifth stages. The coefficients are chosen to be

$$\alpha_1 = 1/4, \quad \alpha_2 = 1/6, \quad \alpha_3 = 3/8, \quad \alpha_4 = 1/2 \quad .$$

The allowable Courant number for the 5 stage scheme is 4.0. This number is increased by smoothing the residuals at each stage.

$$(1 - \epsilon_\xi \delta^2_\xi)(1 - \epsilon_\eta \delta^2_\eta)(1 - \epsilon_\zeta \delta^2_\zeta)\, \overline{\mathbf{R}}_{ijk} = \mathbf{R}_{ijk} \tag{15}$$

Where ϵ_x, ϵ_y and ϵ_z are the smoothing parameters in each direction and are given by, eg.,

$$\epsilon_\xi = \max\left\{0, \frac{1}{4}\left(\frac{CFL}{CFL^*}\frac{\lambda_\xi}{\lambda_\xi + \lambda_\eta + \lambda_\zeta}\right)^2 - 1\right\}$$

Notice in the above equation that the CFL number is scaled by the wave speed in each direction to account for the differences in the maximum allowable time step in that direction. This was not used in the Euler method presented in [5] and is introduced here on consideration of the large disparity in grid sizes in a mesh for solving the Navier-Stokes equations.

2.3 Multigrid Method

In order to further increase the rate of convergence, locally varying time steps are used. A multigrid method based on [17] is implemented. Coarse grids are introduced by eliminating every other grid point on the fine grids. In a vertex scheme values of the flow variables on a coarser grid are taken directly from those on the fine grid at the same grid points. A forcing term is then defined as

$$\mathbf{P}_{2h} = Q^h_{2h}\mathbf{R}_h(\mathbf{W}_h) - \mathbf{R}_{2h}(\mathbf{W}^{(0)}_{2h})$$

where the subscripts h and $2h$ indicate the fine and coarse grids. Q^h_{2h} is a collection operator which forms a weighted average of the residuals on the fine grid in the neighborhood of each mesh point of the coarse grid. To update the solution on a coarse grid the multistage scheme is reformulated as

$$\begin{array}{lcl} \mathbf{W}^{(1)} & = & \mathbf{W}^{(0)}_{2h} - \alpha_1 \Delta t(\mathbf{R}^{(0)}_{2h} + \mathbf{P}_{2h}) \\ & \cdots & \\ \mathbf{W}^{(q+1)} & = & \mathbf{W}^{(0)}_{2h} - \alpha_q \Delta t(\mathbf{R}^{(q)}_{2h} + \mathbf{P}_{2h}) \\ & \cdots & \end{array} \tag{16}$$

where $\mathbf{R}^{(q)}$ is the residual of the q-th stage. In the first stage of the scheme, the addition of $\mathbf{P}_{2h}$ cancels $\mathbf{R}_{2h}(\mathbf{W}^{(0)})$ and replaces it by $Q^h_{2h}\mathbf{R}_h(\mathbf{W}_h)$, with the result that the evolution on the coarse grid is driven by the residual on the fine grid. This process is repeated on successively coarser grids. Finally the correction calculated on each grid is passed back to the next finer grid by linear interpolation along each grid line. In the present work a W-cycle strategy is

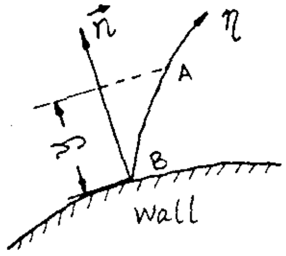

Figure 5: Approximate Normal Distances from Wall

used in each time step. In order to save computational time, the molecular and turbulent viscosity coefficients are evaluated only on the fine grid and frozen on the coarse grids.

In the solution of the Reynolds-averaged Navier-Stokes equations, the robustness of the multigrid method is enhanced by smoothing the corrections from the coarse grids before they are added to the solution on the fine grids. The same factorized smoothing operator as shown in Eqn.(15) is again used with a constant smoothing parameter.

2.4 The Baldwin-Lomax Algebraic Turbulence Model

The Baldwin-Lomax model[14] is used to determine the eddy viscosity in Eqn.(7). In this model, the turbulent heat conductivity k_t in Eqn.(8) is replaced by $c_p\mu_t/Pr_t$, where Pr_t is the turbulent Prantdl number and is fixed as a constant. The eddy viscosity μ_t is given by a two-layer model.

$$\mu_t = \begin{cases} (\mu_t)_{inner} & \text{if } y \le y_{crossover} \\ (\mu_t)_{outer} & \text{if } y > y_{crossover} \end{cases} \tag{17}$$

where y is the normal distance from the wall and $y_{crossover}$ is the smallest value of y at which $(\mu_t)_{inner} = (\mu_t)_{outer}$. Since a general nonorthogonal grid is used in our calculations, the wall distance of a point A on a grid line η shown in Fig. 5 is taken to be its distance to the wall point B projected along the normal to the wall at B. Thus it is only an approximate normal distance in our implementation.

In the inner layer

$$(\mu_t)_{inner} = \rho l^2 |\omega| \tag{18}$$

where

$$l = ky[1 - \exp(-y^+/A^+)] \tag{19}$$

ω is the vorticity

$$|\omega| = \sqrt{(\frac{\partial u}{\partial y} - \frac{\partial v}{\partial x})^2 + (\frac{\partial v}{\partial z} - \frac{\partial w}{\partial y})^2 + (\frac{\partial w}{\partial x} - \frac{\partial u}{\partial z})^2} \tag{20}$$

and

$$y^+ = \frac{\sqrt{\rho_w \tau_{l,max}}\, y}{\mu_w} \tag{21}$$

Notice that the maximum laminar shear stress $\tau_{l,max}$ is used in the above equation instead of the wall shear stress τ_w in the original Baldwin-Lomax formulation. This is to prevent vanishingly small μ_t in the neighborhood of flow separation where the wall stress τ_w is zero.

In the outer region

$$(\mu_t)_{outer} = K C_{cp} \rho F_{wake} F_{Kleb}(y) \tag{22}$$

where

$$F_{wake} = \min\{y_{max} F_{max}, C_{wk} y_{max} U_{diff}^2 / F_{max}\}$$

Y_{max} and F_{max} are determined from the function

$$F(y) = y|\omega|[1 - \exp(-y^+/A^+)] \tag{23}$$

where F_{max} is the maximum value of $F(y)$ that occurs in a profile and y_{max} is the y at which it occurs. F_{Kleb} is the Klebanoff intermittency factor;

$$U_{diff} = (\sqrt{u^2 + v^2 + w^2})_{max} - (\sqrt{u^2 + v^2 + w^2})_{min}$$

where $(\sqrt{u^2 + v^2 + w^2})_{max}$ is the velocity magnitude at y_{max} and $(\sqrt{u^2 + v^2 + w^2})_{min}$ is the minimum velocity magnitude in the profile, which is zero on the wall.

In wakes only the outer formulation is used and the exponential term in Eqn(24) is dropped.

The determination of transition to turbulence is a troublesome matter. In our implementation, transition is either set at a given location or by using a cut-off value for the turbulent eddy viscosity as suggested by Baldwin and Lomax, ie.

$$\mu_t = 0 \qquad \text{if } (\mu_t)_{max} < \mu_\infty C_{MUTM} \tag{24}$$

The various empirical constants in the above model are listed below.

$$\begin{aligned} A^+ &= 26 \\ C_{cp} &= 1.6 \\ C_{Kleb} &= .3 \\ C_{wk} &= 1.0 \\ k &= 0.4 \\ K &= 0.168 \\ C_{MUTM} &= 14 \\ Pr_t &= 0.9 \end{aligned}$$

The implementation of the Baldwin-Lomax model is straight forward in two-dimensions. In three-dimensions ambiguities arise in the corner regions of the cascade blade and end-walls. Fig. 6 shows a cross section of a cascade passage. In the four cor-

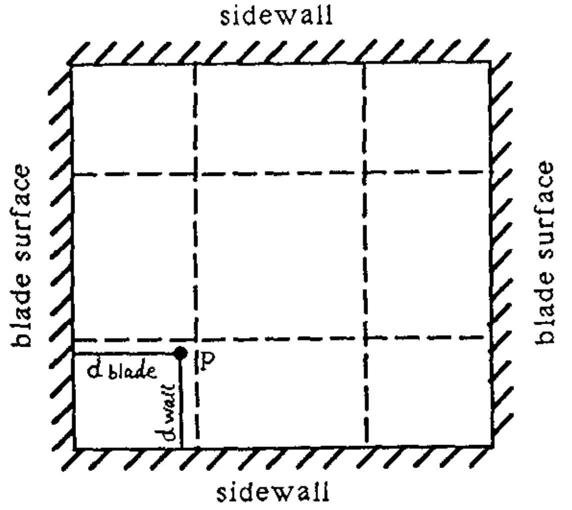

Figure 6: A Cross Section of a Cascade Passage

ners, there are two length scales due to the blade surface and the end-wall. Two turbulent viscosity coefficients $\mu_{t,blade}$ and $\mu_{t,wall}$ can be determined based on the two length scales and the above procedure. In principle, one ought to determine a unique length scale first and then obtain a plausible turbulent viscosity based on the one length scale and the local velocity or time scale of the flow. However, in our applications, because of the difficulty in determining a unique length scale a simple approach is used, in which the two turbulent viscosity coefficients are blended by a weighted averaging according to the distances from the two walls. Thus for the point P

$$\mu_t = \frac{d_{wall}\,\mu_{t,blade} + d_{blade}\,\mu_{t,wall}}{d_{wall} + d_{blade}}$$

where d_{wall} and d_{blade} are the normal distances of P from the blade and the end-wall respectively.

3 Results and Discussions

In order to verify the proposed numerical method, laminar flow over an NACA0012 airfoil, and laminar and turbulent flows over a flat plate are calculated by a two-dimensional version of the the scheme to verify the numerical method. Two and three dimensional calculations for a turbine cascade at design and off-design conditions are then obtained.

3.1 Laminar Flow over the Airfoil NACA 0012

The flow has a freestream Mach number $M_\infty = 0.5$, angle of attack $\alpha = 0°$, and the Reynolds number based on chord length $Re_\infty = 5000$. A 256 × 64 mesh is used. Fig. 7 shows the skin friction coefficient on the airfoil surface. Complete symmetry is achieved with the skin friction curve crossing zero at 0.82 chord point. This marks the start of flow separation from the airfoil surface. The Pressure drag and skin friction drag compare well with results obtained by Radespiel[18] with a different discretization scheme as shown in the following table.

	C_{Dp}	C_{Df}	X_s/c
[18]	0.0227	0.0327	0.81
Present Method	0.0226	0.0329	0.82

Fig. 8 shows some particle traces around the airfoil. The recirculating vortices are seen near the trailing edge. Fig. 9 is the convergence history for this case. Monotonic convergence is achieved and the scheme gives an engineering acceptable solution within only 50 cycles.

3.2 Laminar and Turbulent Flow over a Flat Plate

In these calculations, the free stream Mach number is set to 0.3 to approximate incompressible flow. Laminar flow at Reynolds number $Re = 35000$ is obtained. Fig. 10 shows the calculated surface skin friction and that by Blasius in logarithmic scales.

A good check is the similarity profile offered by the Blasius solution. Fig. 11 shows the calculated velocity profile as scaled by the Blasius similarity law at about 10%, 20%,. . .,and 90% chord length downstream of the leading edge. All of the data points collapse into a single curve on the Blasius velocity profile. Similarity is also obtained with the vertical velocities.

Turbulent flow over the same flat plate at $Re = 6 \times 10^6$ is calculated. Fig. 12 is the calculated surface skin friction plotted in logarithmic scale compared with the 1/5 law of Prandtl. The skin friction jumps up at transition and then follows the 1/5 law closely towards the end of the plate.

Fig. 13 shows the turbulent similarity velocity profile at different streamwise locations. Regions of laminar sublayer, the logarithmic law of the wall and the wake are distintly captured.

3.3 Flow Through a Turbine Cascade

Notwithstanding the success of the algebraic model for the flat plate, the same model should not be expected to be equally applicable to other turbulent flows. The above results confirm, however, the proper implementation of the Baldwin-Lomax model. In this section the importance and limitations of solving the Navier-Stokes equations is demonstrated in calculations of the flow through a low pressure turbine cascade[12] at its design and off-design conditions.

Fig. 14 is the two-dimensional mesh with 209 × 65 grid points used in the calculations. The mesh is initially generated by an elliptic method and then stretched in the blade to blade direction to provide grid point clustering near the blade surfaces. The first grid point is taken to be 1.5×10^{-4} axial chord length away from the blade surface. In the three-dimensional calculations, only half of the blade span is used since the blade passage has a symmetric divergence of 6 degrees on the sidewalls. A $209\times65\times33$ mesh is generated by stacking the two-dimensional mesh in the spanwise direction. The z coordinate of the grid points are stretched along spanwise grid lines to make the mesh conform to the endwall and provide clustering near the wall. Since this cascade has a large aspect ratio(1.818 at the exit) and a pitch-chord ratio of 0.564, the spanwise resolution provided by the 33 grid points in half span is in fact rather poor compared to the blade to blade passage. The smallest grid size near the endwall used in this work is only 2.8×10^{-3} axial chord length.

In all the calculations, the Baldwin-Lomax algebraic model described in the previous section is used. Transitions are set at specific locations on the blade surfaces. On the side walls, experimental data in Hodson and Dominy [12] suggest that the flow is turbulent at the entrance and transitional at the exit. In the calculations, the flow is assumed to be fully turbulent on all of the endwalls. The endwall velocity profile at the entrance is specified by experimental data provided in [12].

3.3.1 Flow at the Design Condition

At its design condition this cascade has an exit isentropic Mach number of 0.7, an incidence angle of 38.8 degrees, and an isentropic exit Reynolds number $Re = 2.9 \times 10^5$. Fig. 15 reproduces from [5] the isentropic Mach number distribution at mid-span obtained with a three-dimensional Euler method. It was explained in [5] that the slight discrepancy between calculation and experiment on the aft portion of the upper surface was due to a small separation bubble, which was observed in Hodson and Dominy's experiment[12].

In view of the large amount of computer memory and CPU time needed by a full three-dimensional Navier-Stokes calculation, some computations were first carried out with a two-dimensional version of the current method. Fig. 16 is the isentropic Mach number distribution at mid-span calculated by the two-dimensional code. Compared to Fig. 15, the two-dimensional result underpredicts the isentropic Mach number by quite a margin due to the fact that it does not account for the divergence of the endwalls. However, the small hump in the aft portion of the suction surface pressure distribution that was observed in the experiment but missed by the inviscid calculation is now captured by the viscous code.

The separation bubble on the back of the cascade blade is confirmed by the skin friction distribution shown in Fig. 17. This separation starts at about 80% axial chord and ends at about 90% axial chord, which agrees with the experimental location obtained by oil flow in[11, 12]. It is due to this separation bubble that the isentropic Mach number in that region exhibits higher values than the inviscid solution. A small leading edge separation bubble which was observed in experiment on the suction surface[12], however, is not found in this calculation, although the skin friction does show a spiked low value near the leading edge. This is most likely due to the inability of the mesh to resolve the thin boundary layer near the leading edge. On the pressure surface incipient separation exists from about 15% axial chord to about 20% axial chord. Hodson and Dominy[11] estimated that this was from 12% to 20% blade surface distance based on oil flow visualization.

Transition in this calculation is set at 0.88 axial chord on the suction surface and 0.2 axial chord on the pressure surface in view of the approximate transition locations observed in experiment. Some adjustments of these locations were performed so that the pressure distribution agreed better with the experimental data. The original transition criterion by Baldwin and Lomax did not give good results. Such manual adjustment on transition and the turbulence model itself present the major uncertainties in the calculation.

The two-dimensional calculations captures most of the viscous features of the flow at mid-span, despite the inaccuracy caused by assuming no endwall divergence. Fig. 18 shows the isentropic Mach number at mid-span with the three-dimensional version of the code. Clearly this problem is rectified. Fig. 19 shows the skin friction distribution at mid span. Compared to the two-dimensional solution in Fig. 17, the three-dimensional solution does not predict a true separation bubble on the suction surface, rather it predicts a small region of near separation flow. Nonetheless, the small hump in the isentropic Mach number distribution shown in Fig. 18 is still closely reproduced.

The three-dimensional viscous calculation with the rather fine $209 \times 65 \times 33$ mesh needs about 300 Megabytes of memory in double precision and takes about 12 hours of CPU time on a single processor on a Convex C220 to march 200 time steps. In comparison, the two-dimensional code needs only 10 Megabytes of memory and less than 20 minutes of CPU time for the same number of time steps but with better convergence. Fig. 20 shows the convergence history for the two and three-dimensional calculations. The parameters in the numerical scheme have not been optimized for the three-dimensional calculations due to constraints in computer time.

The effect of the side wall boundary layer is closely related to secondary flow development in the cascade passage. It was shown in [5] that given the entrance side-wall boundary layer profiles, the Euler model was capable of predicting the qualitative features of the secondary flow vortices due to inviscid convection. Fig. 21 contains a reproduction of the spanwise variation of pitchwise mixed-out flow angle at 140% axial chord along with those obtained by experiment[12] and the current Navier-Stokes code. There is a large overturning near the wall. This overturning is then followed by an underturning some distance into the flow field. This is due to the induced velocity by the passage vortex. In the inviscid solution the underturning of the flow was predicted with the right magnitude but a displaced location. The discrepancy was attributed to the fact that the Euler model does not account for the boundary layer growth in the cascade passage due to the diffusive effects of viscosity. The Navier-Stokes solution shown in Fig. 21 seems to confirm this diffusive effect. However, the predicted magnitude of the underturning is not as large as that of the inviscid solution.

Notice also the difference between the inviscid and viscous solutions near the endwall in Fig. 21. The overturning is reduced in the viscous solution as compared to the steady increase in the inviscid solution. The blade to blade pressure gradient forces the low energy flow in the boundary layer to turn more than the inviscid core flow, thus forming the passage vortex. But very near the wall viscous effects retarts this overturning mechanism. The experimental results from Hodson did not provide data very near the wall, but the existence of reduced overturning was pointed out.

If the endwall is regarded as a flat plate with laminar flow, a grid size of 2.8×10^{-3} axial chord length would correspond to an $\eta = \sqrt{Re}\, y/\sqrt{x}$ of 1.5 in the Blasius velocity profile at the end of the plate with Reynolds number 2.9×10^5. With grid stretching, the 4th grid point would give $\eta > 6$, which is outside the boundary layer. It must be remembered that the flow over the endwall is turbulent, which will need an even smaller grid size to have at least one grid point in the laminar sublayer region. On this consideration, it is doubtful whether we have adequate resolution for the endwall boundary layers with the current grid. Nevertheless, the predicted spanwise variation of pitchwise mixed-out flow angle shown in Fig. 21 seem to agree with the experimental data. More detailed examination of the endwall boundary layer, its interaction with the blade surface and the development of secondary flows must be pursued.

3.3.2 Flow at an Off-Design Condition

Fig. 22 shows the inviscid pressure distribution obtained in [5] at $-20.3°$ incidence relative to the design condition. In this case there is a large separation bubble on the pressure surface. Because of this separation the inviscid solution shows a large suction peak and then a steep diffusion as compared to the smaller suction followed by a long flat curve measured in experiment. Fig. 23 is the solution obtained with the two-dimensional Navier-Stokes code. The flat region of pressure distribution due to separation is reproduced with surprisingly good accuracy, considering the uncertainties involved in the calculation. Transition to turbulence in this calculation is set at 0.84 axial chord on the suction surface and 0 axial chord on the pressure surface. Fig. 24 shows the skin friction on the blade. The pressure surface separation bubble can be clearly seen. The flow separates at about 3% axial chord and then experiences transition and reattaches at about 58% axial chord. Hodson and Dominy[13], however, found that the separation is of a smaller length from 5% to 45% axial chord. This may explain why the calculated isentropic Mach number tends to curve upwards compared to the experimental data. comparison with results by other turbulence models would be desirable. Fig. 25 shows the velocity vectors below the pressure surface. The large recirculation is evident.

On the suction surface, there is a small separation bubble on the back of the blade. This is confirmed by the skin friction plot and by the small hump in isentropic Mach number distribution shown in Fig. 23. Fig. 26 displays the velocity vectors in that region. An incipient separation can be seen.

Although a steady state solution was achieved for this case with the two-dimensional code, it was not obtained with the three-dimensional program on the $209 \times 65 \times 33$ mesh. Calculations show quite fast convergence on a coarse mesh with $105 \times 33 \times 17$ grid points. When the solution on the coarse grid is interpolated onto the fine grid, the fine grid solution converges to a certain point and then starts to oscillate with the maximum residuals occurring in the lower wall separation region. This may be related to the nature of the flow separation and the properties of turbulence modeling. Fig. 27 shows the isentropic Mach number at mid-span obtained by the three-dimensional code at one instant. Fig. 28 is the skin friction at mid-span, which reveals that the flow on the pressure surface separates, reattaches and then separates again. The same trend seems to be also present in the converged two-dimensional solution. It should be pointed out that Hodson and Dominy did not provide detailed skin friction measurement for this cascade, nor do the authors have knowledge of any computational results by other methods. It would be very desirable to compare results by other methods and with other turbulence models.

4 Concluding remarks

A vertex-based finite volume method with a multi-stage time stepping scheme for the Reynolds-averaged Navier-Stokes equations is presented for calculating three-dimensional cascade flows. The program has been validated by calculating laminar flow over a NACA0012 airfoil, and laminar and turbulent flows over a flat plate.

The method has been applied to a three-dimensional low pressure turbine cascade which was studied by an Euler method. Clear improvements were achieved over the Euler solutions for flows with separation at both design and off-design conditions. A 209×65 mesh in the blade to blade section with a minumum grid size of 1.5×10^{-4} axial chord is adequate to resolve the boundary layer over the blade surfaces. Skin friction plots show the separation bubbles which were observed in experiment. However, the locations of transition and turbulence modeling pose uncertainties to the calculations.

Although the smallest grid size used in the calculation over the endwall does not seem to be small enough to adequately resolve the turbulent endwall boundary layer, the predicted variation of pitchwise mixed-out exit flow angle compare reasonably well with experimental data in both strength and location. More detailed studies on the interaction between the blade and the endwall boundary layers and the development of secondary flows are needed.

Despite the uncertainties involved in Reynolds-averaged Navier-Stokes calculations with turbulence modeling, the proposed method provides a viable tool for flow analysis and engineering design of turbomachinery cascades.

References

[1] Denton, J. D., "An Improved Time-Marching Method for Turbomachinery Flow Calculation", J. of Engineering for Gas Turbines and Power, Vol. 105, July 1983.

[2] Smith, W. A., and Caughey, D. A., "Multigrid Solution of Inviscid Transonic Flow Through Rotating Blade Passages", AIAA Paper 87-0608.

[3] Holmes, D. G., and Tong S. S., "A Three-Dimensional Euler Solver for Turbomachinery Blade Rows", J. of Engineering for Gas Turbines and Power, Vol. 107, April 1985.

[4] Jameson, A., and Liu, F., "Multigrid Calculations for Cascades", in *Lecture Notes in Physics* 323, Dwoyer D. L. and Hussaini M. Y. and Voigt R. G. eds., Springer-Verlag, 1989.

[5] Liu, F. and Jameson, A., "Multigrid Euler Calculations for Three-Dimensional Cascades", AIAA Paper 90-0688.

[6] Hah, C., "Calculation of Three-Dimensional Viscous Flows in turbomachinery with an Implicit Relaxation Method", Journal of Propulsion, Vol. 3, No.5, 1987

[7] Chima, R. V., "Explicit Multigrid Algorithm for Quasi-Three-Dimensional Viscous Flows in turbomachinery", Journal of Propulsion, Vol. 3, No.5, 1987

[8] Davis R. L., Ni, R.-H. and Carter, J. E., "Cascade Viscous Flow Analysis Using the Navier-Stokes Equations", Journal of Propulsion, Vol. 3, No.5, 1987

[9] Choi, D. and Knight C. J., "Computation of Three-Dimensional Viscous Linear Cascade Flows", AIAA Journal, Vol. 26, No.12, 1988

[10] Dawes, W. N., "Development of a 3-D Navier-Stokes Solver for Application to all Types of Turbomachinery", ASME Paper 88-GT-70, 1988.

[11] Hodson H. P. and Dominy R. G., "Boundary Layer Transition and Separation Observed near the leading Edge of a High Speed Turbine Blade", ASME J. Eng. for G.T. & Power, Vol 107, Jan. 1985

[12] Hodson H. P. and Dominy R. G., "Three-Dimensional Flow in a Low Pressure Turbine Cascade at its Design Condition", ASME paper 86-GT-106, 1986

[13] Hodson H. P. and Dominy R. G., "The Off-Design Performance of a Low Pressure Turbine Cascade", ASME paper 86-GT-188, 1986

[14] Baldwin, B. S. and Lomax, H., "Thin Layer Approximation and Algebraic model for separated Turbulent Flows", AIAA Paper 78-257, 1978.

[15] Liu, F. "Numerical Calculation of Turbomachinery Cascade Flows", Ph.D. Thesis, Princeton University, June, 1991.

[16] Martinelli, L., "Calculations of Viscous Flows with a Multigrid Method", Ph.D. Thesis, Department of Mechanical and Aerospace Engineering, Princeton University, 1987.

[17] Jameson, A., "Solution of the Euler Equations by a Multigrid Method", Applied Math. and Computation, Vol. 13, 1983, pp.327-356.

[18] Radespiel, R., "A Cell-Vertex Multigrid Method for the Navier-Stokes Equations", NASA TM-101557.

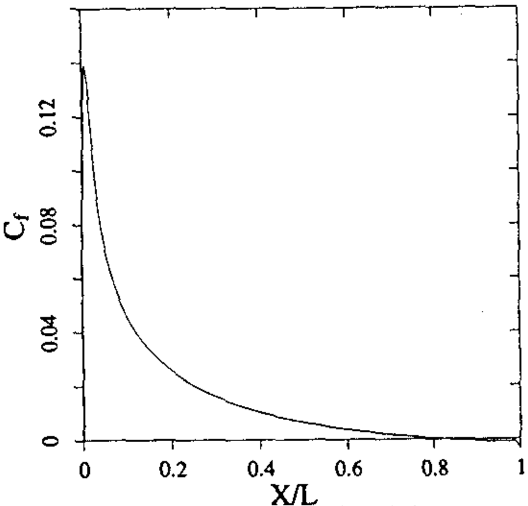

Figure 7: Skin Friction Coefficient on a NACA0012 Airfoil

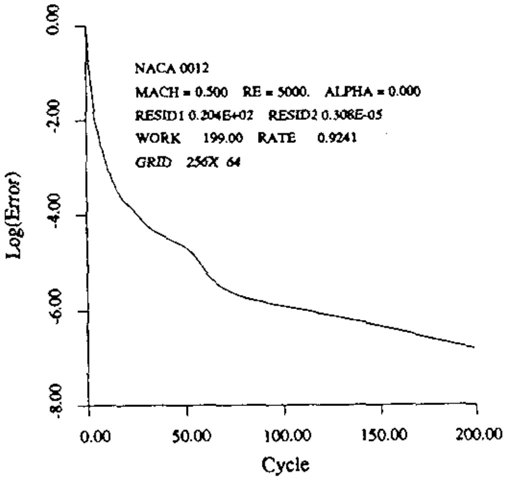

Figure 9: Convergence History for a NACA0012 Airfoil

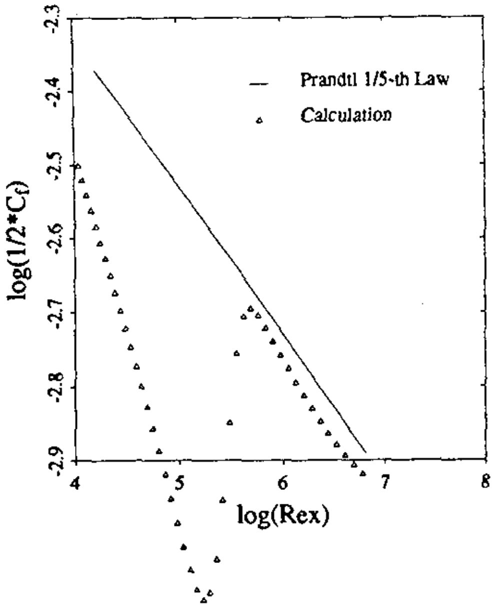

Figure 12: Turbulent Skin Friction over a Flate Plate

Figure 8: Particle Traces over a NACA0012 Airfoil

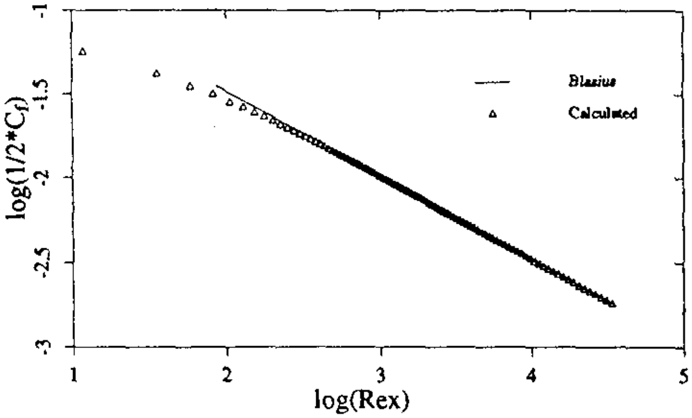

Figure 10: Laminar Skin Friction Coefficient over a flate plate

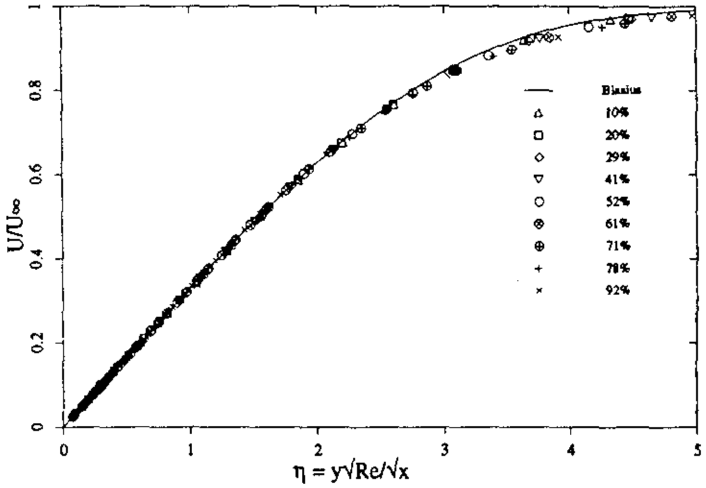

Figure 11: Laminar Boundary Layer Velocity Profile Over a Flat plate

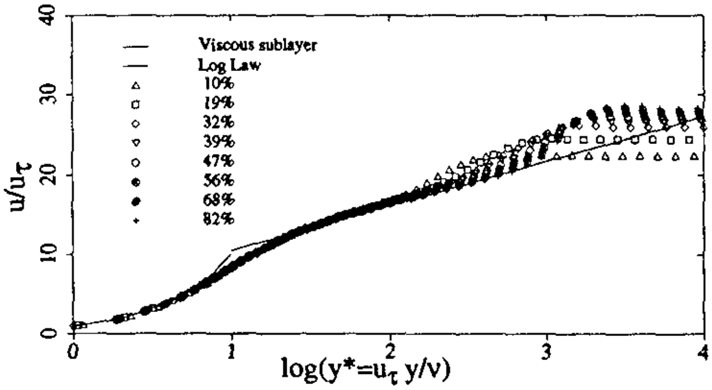

Figure 13: Turbulent Boundary Layer Velocity Profile over a Flate Plate

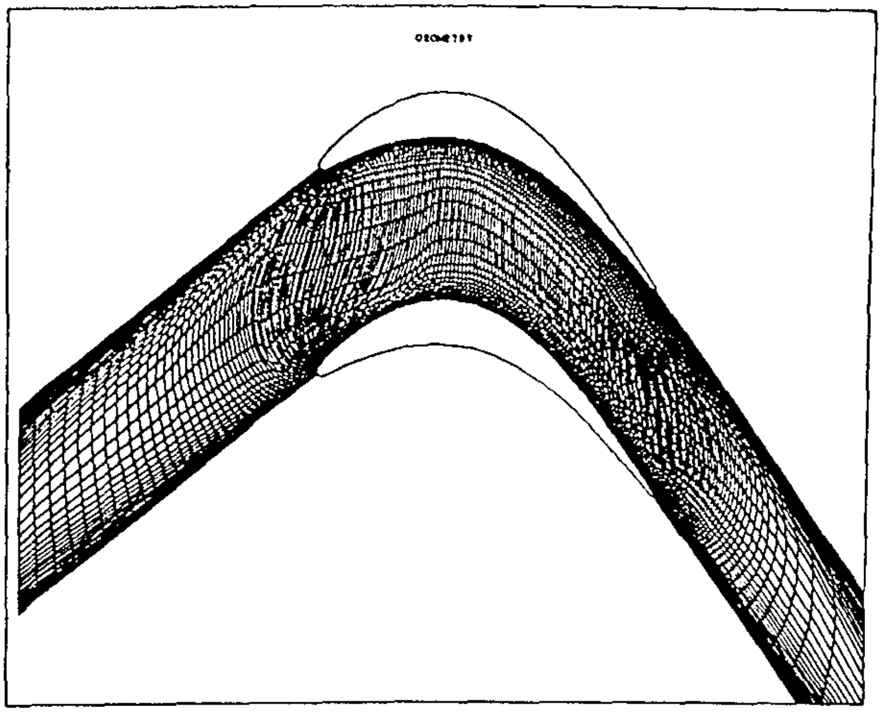

Fig. 14: H-mesh of 208 × 64 cells for a Low Pressure Turbine Cascade

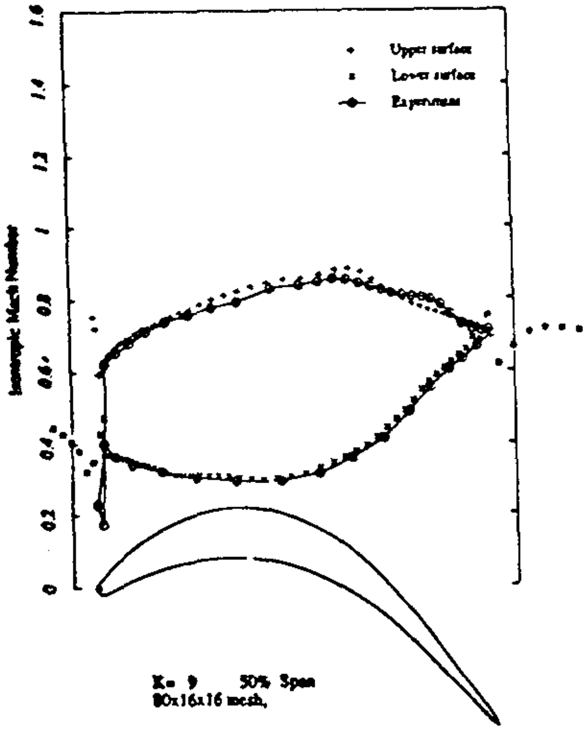

Fig. 15: Isentropic Mach Number at Mid-span, 3D Euler Solution

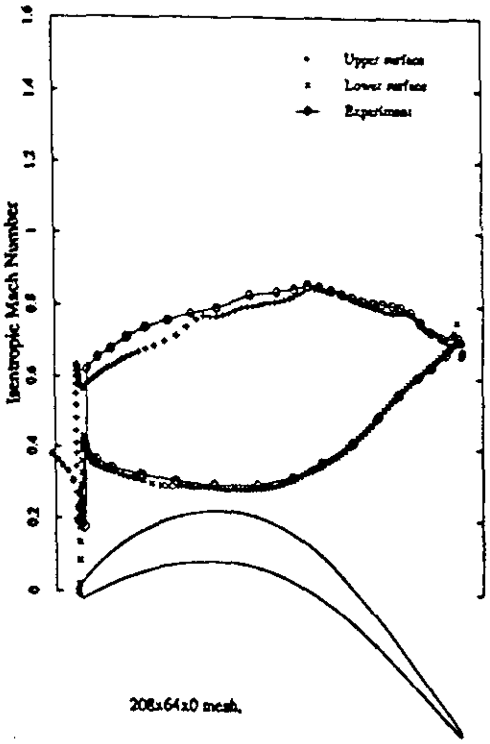

Fig. 16: Isentropic Mach Number at Mid-span, 2D Navier-Stokes Solution

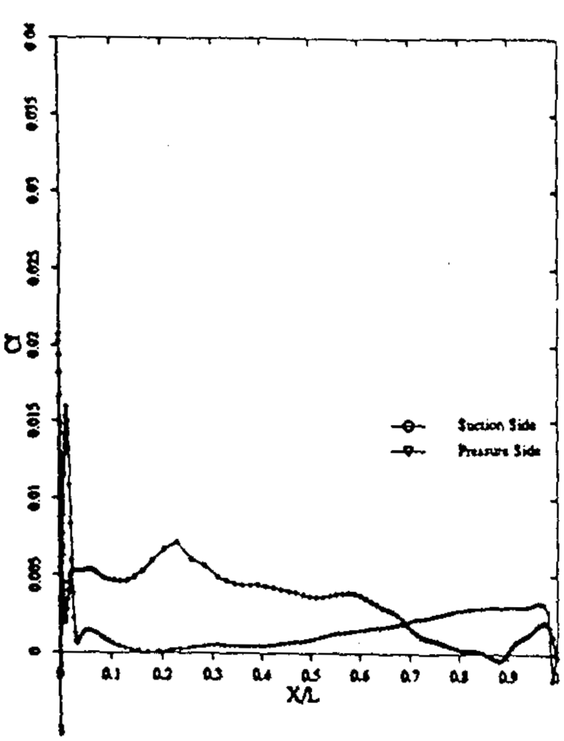

Fig. 17: Skin Friction Distribution at Mid-span, 2D Navier-Stokes Solution

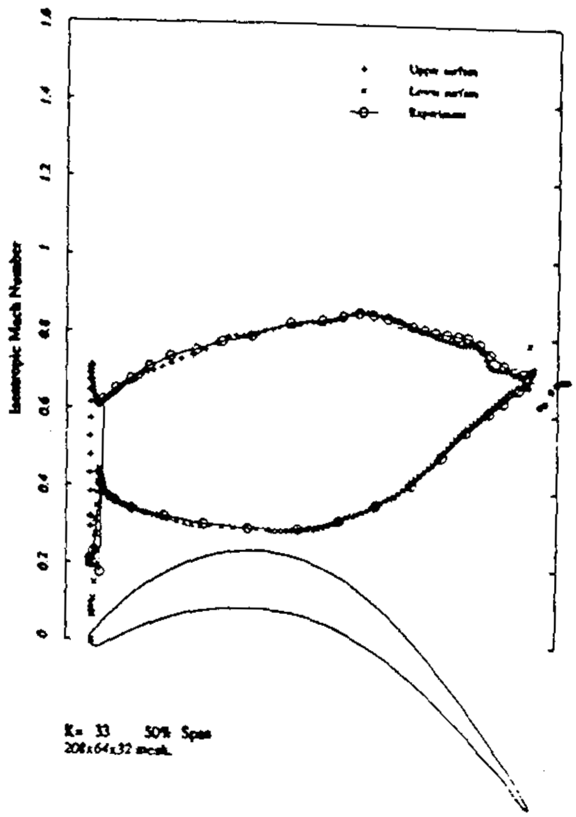

Fig. 18: Isentropic Mach Number at Mid-span, 3D Navier-Stokes Solution

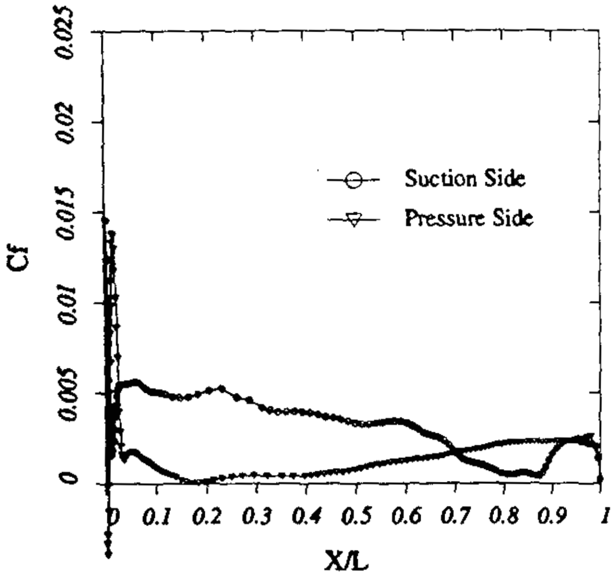

Fig. 19: Skin Friction Distribution at Mid-span, 3D Navier-Stokes Solution

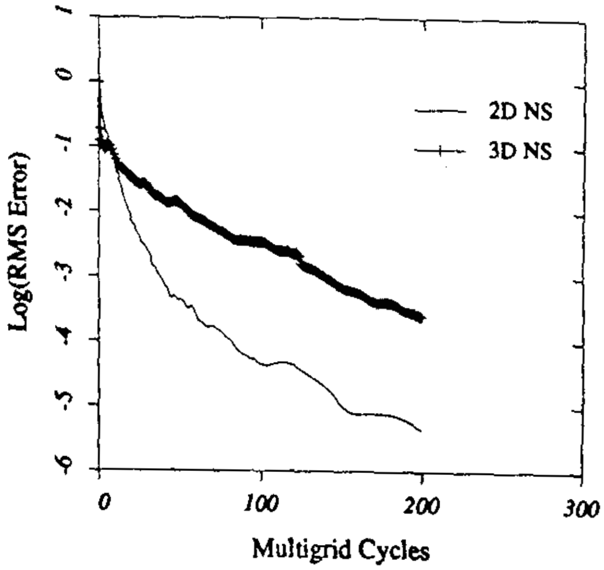

Fig. 20: Convergence History of Navier-Stokes Calculations

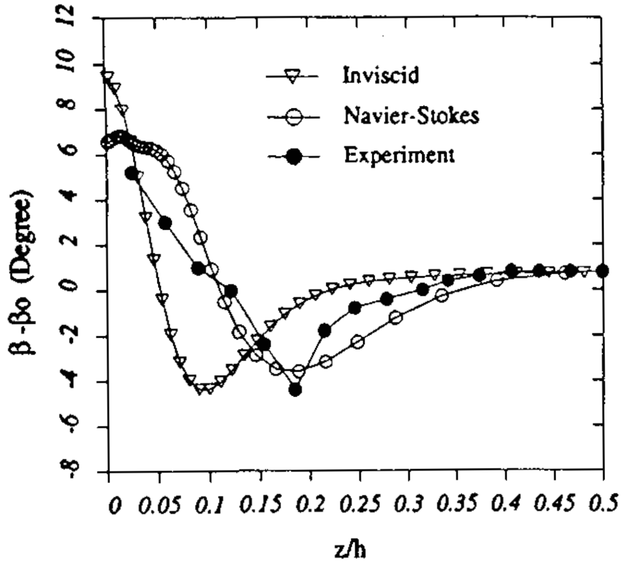

Fig. 21: Spanwise Variation of Pitchwise Mixed-out Flow Angle at 140% Axial Chord

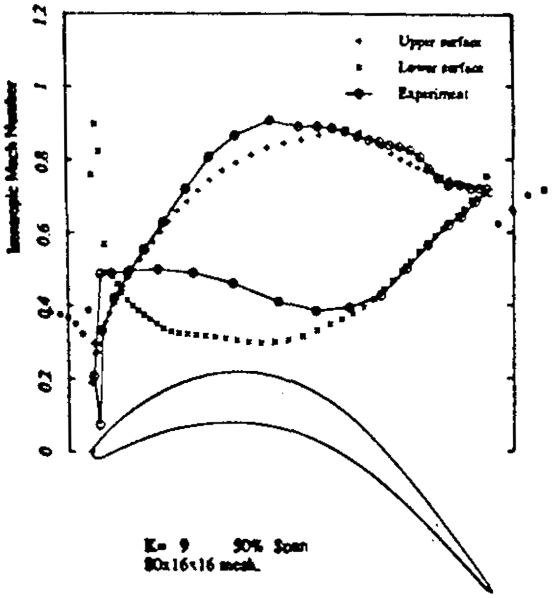

Fig. 22: Isentropic Mach Number at Mid-span at Off Design Condition, Euler Solution

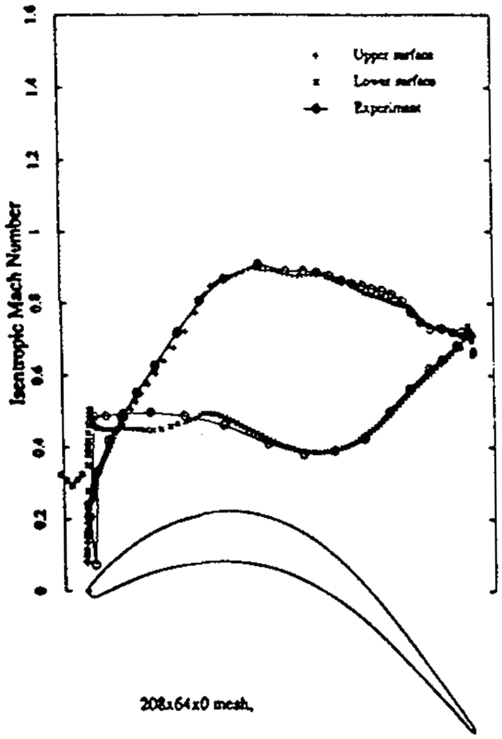

Fig. 23: Isentropic Mach Number at Mid-span at Off Design Condition, 2D Navier-Stokes Solution

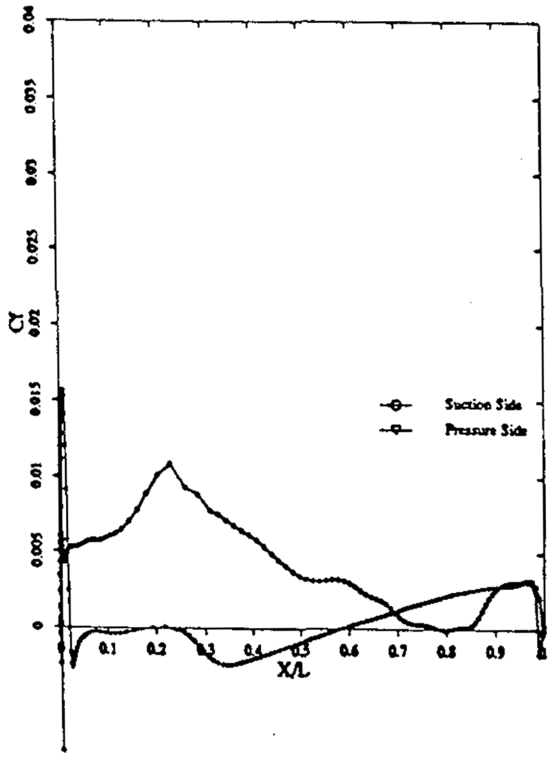

Fig. 24: Skin Friction Distribution at Mid-span at Off-design condition, 2D Navier-Stokes Solution

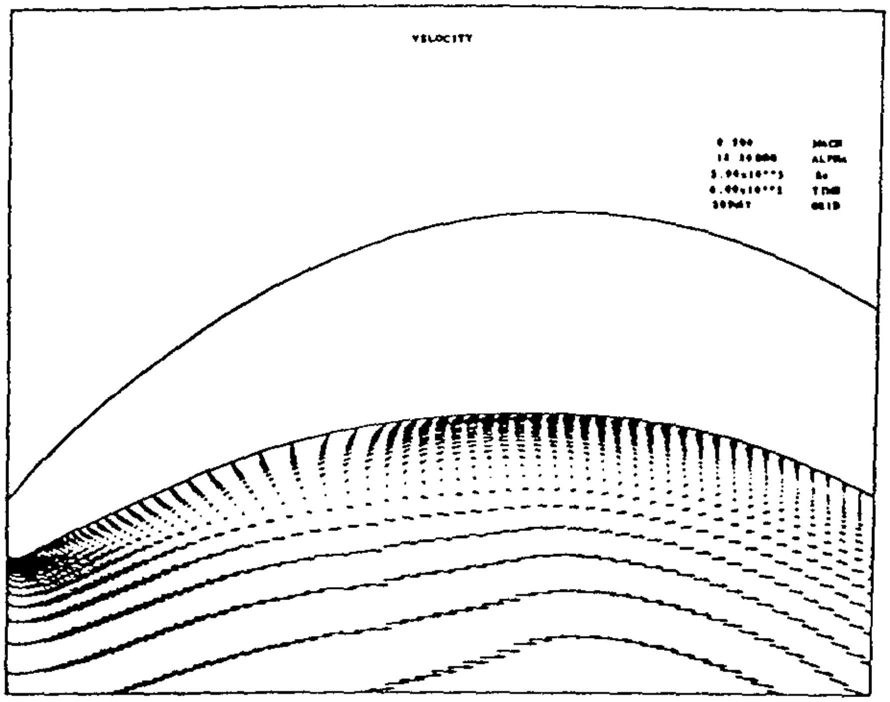

Fig. 25: Velocity Vector Field on the Lower Surface of the Cascade Blade

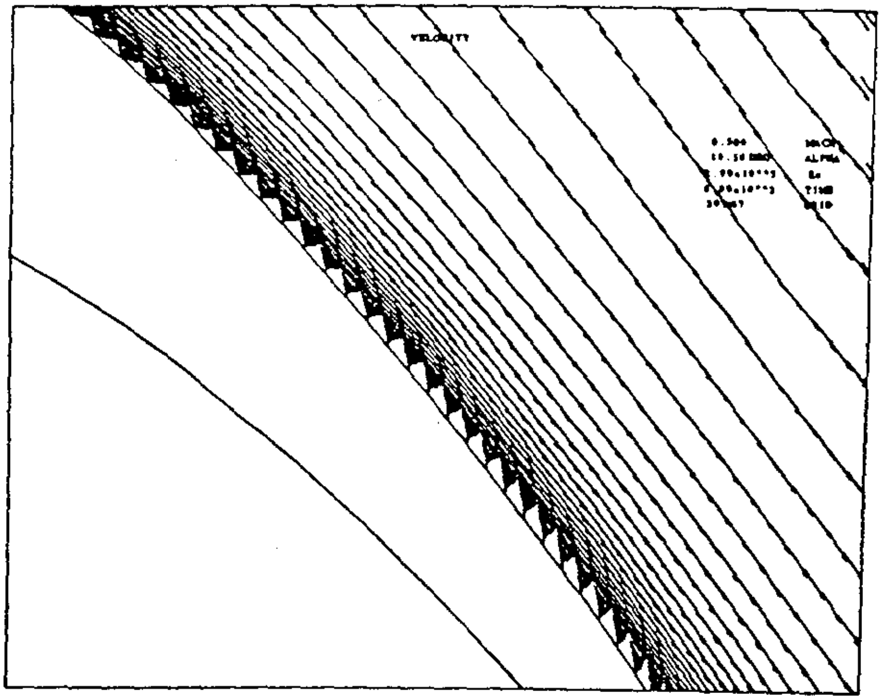

Fig. 26: Velocity Vector Field on the Upper Surface of the Cascade Blade

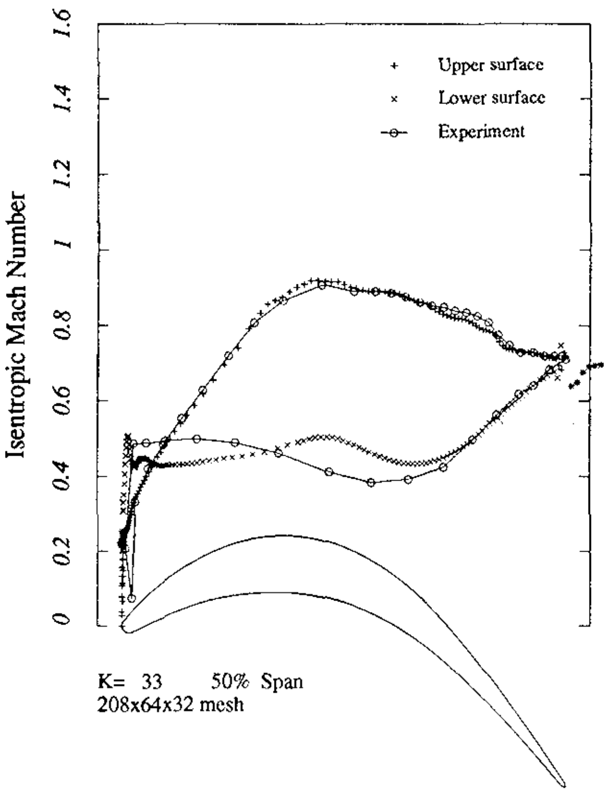

Fig. 27: Isentropic Mach Number at Mid-span at Off Design Condition, 3D Navier-Stokes Solution

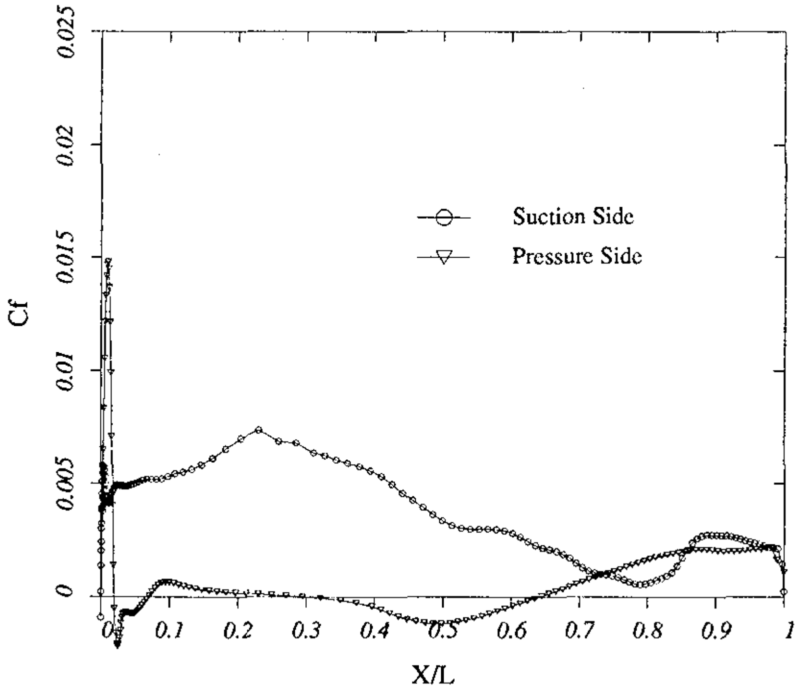

Fig. 28: Skin Friction Distribution at Mid-span at Off-design condition, 3D Navier-Stokes Solution